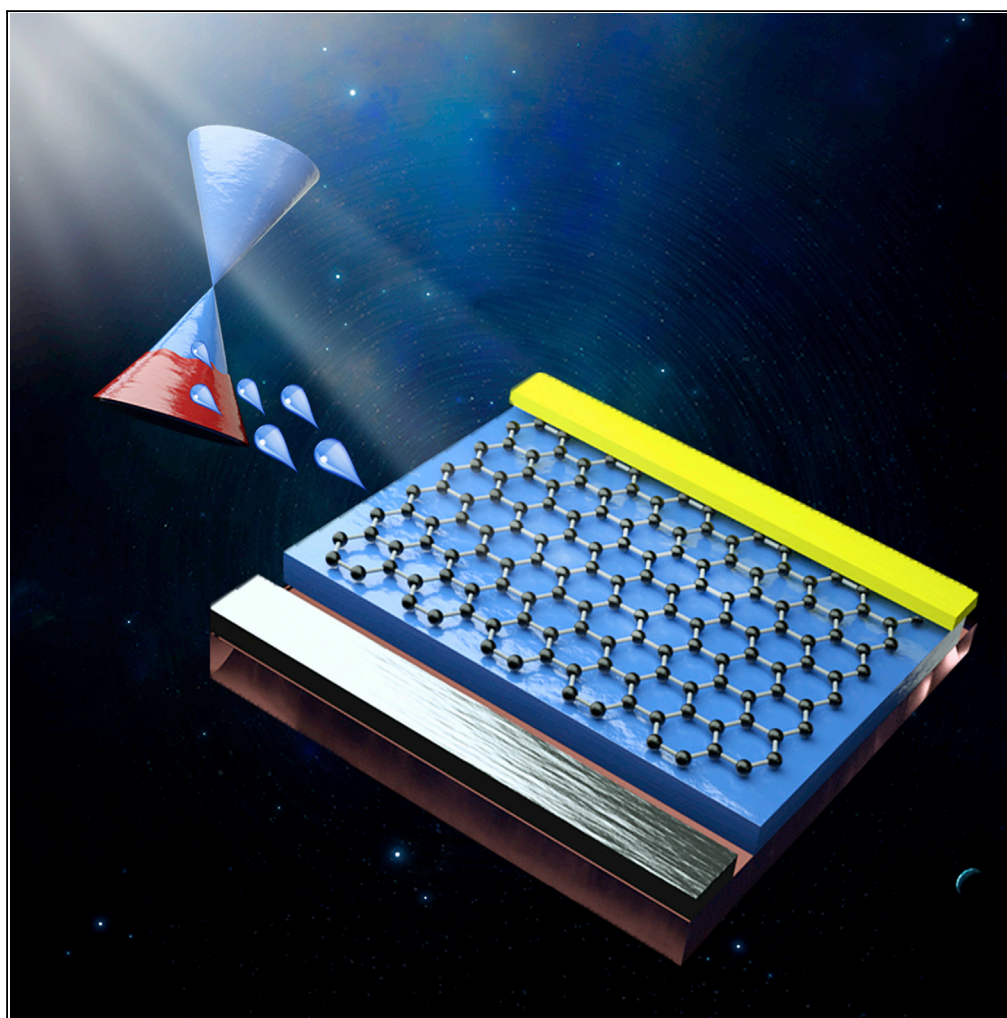**Article**

Ultra-high Photovoltage (2.45 V) Forming in Graphene Heterojunction via Quasi-Fermi Level Splitting Enhanced Effect

Lemin Jia, Wei Zheng, Richeng Lin, Feng Huang

zhengw37@mail.sysu.edu.cn

HIGHLIGHTS

An open-circuit voltage up to 2.45 V is achieved by the graphene heterojunction device

An efficient band assembly is designed to induce the larger quasi-Fermi level splitting

An EQE as high as 56.1% (172 nm) and a rise time as short as 45 ns are achieved

The adopted effect provides a referential way for various photovoltaic devices

Article

Ultra-high Photovoltage (2.45 V) Forming in Graphene Heterojunction via Quasi-Fermi Level Splitting Enhanced Effect

Lemin Jia,[1] Wei Zheng,[1,2,*] Richeng Lin,[1] and Feng Huang[1]

SUMMARY

Owing to the fast response speed and low energy consumption, photovoltaic vacuum-ultraviolet (VUV) photodetectors show prominent advantages in the field of space science, high-energy physics, and electronics industry. For photovoltaic devices, it is imperative to boost their open-circuit voltage, which is the most direct indicator to measure the photoelectric conversion capability. In this report, a quasi-Fermi level splitting enhanced effect under illumination, benefiting from the variable Fermi level of graphene, is proposed to significantly increase the potential difference up to 2.45 V between the two ends of p-Gr/i-AlN/n-SiC heterojunction photovoltaic device. In addition, the highest external quantum efficiency of 56.1% (under the VUV irradiation of 172 nm) at 0 V bias and the ultra-fast photoresponse of 45 ns further demonstrate the superiority of high-open-circuit-voltage devices. The proposed device design strategy and the adopted effect provide a referential way for the construction of various photovoltaic devices.

INTRODUCTION

Vacuum UV (VUV, 10–200 nm) detection technology plays an indispensable role in modern science. The monitoring of space weather such as solar wind (Baker et al., 2004; Baker, 2002; Shea et al., 2006), the measurement and diagnosis of VUV sources like VUV free electron lasers (Braune et al., 2016; Sorokin et al., 2019), and the control of VUV sources in the electronics industry like high-resolution lithography (Li et al., 2017; Richter et al., 2002) have become the main driving force for the development of VUV photodetectors (PDs). VUV filterless PDs based on ultrawide-band-gap semiconductor have become a research hotspot in recent years owing to the advantages of miniaturization and integration (Balducci et al., 2005; BenMoussa et al., 2009, 2013; Li et al., 2006; Soltani et al., 2008). In addition to the high responsivity PDs have always pursued, ultra-fast response speed and low power consumption are also the indicators particularly important especially for deep space applications. At present, most widely reported VUV PDs are photoconductive devices that have realized ultra-high photoresponsivity through the gain mechanism (Zheng et al., 2015, 2018c, 2018d) at the expense of response speed and in demand of electrical input (such as a certain bias). Fortunately, in these two aspects, photovoltaic (PV) VUV PDs with vertical structure (Ouyang et al., 2018; Zheng et al., 2018a) have significant advantages. For one thing, since the photo-generated carriers can be efficiently separated by the built-in electric field and collected by the charge-selective transport layer in the thinner depletion layer, the PV device can easily realize ultra-fast response speed (Michel et al., 2010; Tsukazaki et al., 2004; Xu et al., 2018). For the other thing, a PV device operating at zero bias can directly output an electrical signal, which not only reduces the power consumption of the entire detection system but also enhances the ability of electrical signals to reproduce optical signals, hence reducing the distortion of the final imaging.

It is well known that open-circuit voltage, one of the most critical performance indicators of PV devices, can measure the photoelectric conversion capability of the devices. Its value is equal to the photovoltage when the circuit current is zero. A larger open-circuit voltage means a larger voltage signal output and a higher external quantum efficiency. In theory, the maximum open-circuit voltage that a device can generate depends on the maximum split of quasi-Fermi level within the absorber layer, which is limited by the contact potential difference at the junction interface (Battaglia et al., 2016). However, in reality, the open-circuit voltage of the device is also related to the dynamics of the loss mechanism, including bulk material recombination and various interface recombinations (Stolterfoht et al., 2018). Therefore, efficient band assembly is the most critical way to obtain high open-circuit voltage.

[1]State Key Laboratory of Optoelectronic Materials and Technologies, School of Materials, Sun Yat-sen University, Guangzhou 510275, China

[2]Lead Contact

*Correspondence:
zhengw37@mail.sysu.edu.cn

Graphene with unique properties has been widely used in the construction of modern semiconductor devices such as PDs and PV cells (Bonaccorso et al., 2015; Novoselov et al., 2012). The reported VUV transmittance of up to 96% (Zheng et al., 2018a) indicates that it is a preferred choice for transparent window layers. More importantly, in addition to high mobility, graphene is featured by a low density of states near the Dirac point, which means that its Fermi level can be changed not only by chemical doping, but also by electrical injection (Das Sarma et al., 2011). Therefore, we suppose that, when graphene is used as the hole collection layer, it will help to form a larger splitting of quasi-Fermi level under illumination.

In this report, an efficient band assembly using graphene is implemented to enhance the contact potential difference and thus to induce the greater splitting of quasi-Fermi level in the absorber layer under illumination. Intrinsic-type AlN with ultrawide direct band gap ($\sim$6.2 eV) (Bacaksiz et al., 2015) and ultra-high radiation resistance (BenMoussa et al., 2008), n-type doped 4H-SiC with relatively smaller electron affinity ($\sim$3.1 eV) (Brauer et al., 1996) and high electron saturation drift velocity, and graphene are selected as the absorber layer, electron collection layer, and hole collection layer, respectively. Interestingly, the maximum open-circuit voltage of the constructed p-Gr/i-AlN/n-SiC heterojunction PV device is up to 2.45 V. We attribute this result to the variable Fermi level of graphene and the relatively small electron affinity potential of SiC, which make the potential difference formed at both ends of the device be significantly enhanced. Moreover, voltage loss caused by non-radiative recombination is suppressed due to the growth of lattice-matched high-quality crystals (a_{AlN} = 3.11 Å, a_{4H-SiC} = 3.08 Å, lattice mismatch less than 1% in [0001] direction) (Park et al., 1994; Zoroddu et al., 2001). To further confirm the quasi-Fermi level splitting enhanced effect achieved by graphene, the graphene-free devices that use metals directly as translucent electrodes were constructed. The maximum open-circuit voltage obtained from these devices is only 2.15 V. Finally, we tested the detection performance of the device as a VUV PD. The high external quantum efficiency (EQE) of the device and its ultra-fast response speed (R_{max} = 79.6 mA/W, EQE_{max} = 56.1%, rise time $\approx$ 45 ns, decay time $\approx$ 5 μs) further demonstrate the availability of the proposed device design strategy. This work has tapped more possibility for the application of PV devices to the fields such as space solar cells and UV cameras.

RESULTS AND DISCUSSION

Construction of the PV Device

To obtain a high-quality absorber layer to reduce the trap-assisted recombination, we have hetero-epitaxially grown a high-quality AlN film ($\sim$100 nm) on an n-type 4H-SiC single crystal substrate (electron density is about 10^{18} cm^{-3}) by Metal-organic Chemical Vapor Deposition (MOCVD) (see Transparent Methods). The cross-sectional view of scanning electron microscope (SEM) image in Figure 1A indicates that the film is extremely uniform and appears to have crystalline features over a thickness range of 101.8 nm. The X-ray diffraction spectra and Raman spectrum verify that both AlN and SiC grow along the c-axis and long phonon lifetime and n-type doping of SiC, respectively (Figure S1). The high-resolution transmission electron microscope (HRTEM) pattern was carried out on the AlN/SiC interface in Figure 1B, demonstrating that SiC and AlN have consistent crystal orientation and good lattice matching, which contributes to reduce the photovoltage loss caused by dislocation defects. The characteristic peak of transverse optical (TO) vibration mode in infrared absorption spectra of AlN (Figure 1C) further illustrates the high crystallinity of the absorber layer. The photoluminescence spectrum (Figure 1D) was measured at room temperature, from which an extremely clear band edge emission of the AlN film without any impurity peak could be noticed at 206.5 nm, suggesting that the high-quality AlN film has excellent selective absorption characteristics for VUV light.

After obtaining an epitaxial AlN film on a 4H-SiC single crystal substrate, the high-quality graphene (naturally slight p-type) grown by CVD (Wood et al., 2011) was formed on the AlN surface that serves as a transparent conductive window (Bae et al., 2010; Li et al., 2009) via a wet transfer method (see Transparent Methods). The Raman mapping image shows the spatial uniformity of graphene on AlN film (Figure S2). For the sake of the ohmic contact between the metal and the semiconductor and to obtain a desired electrical output, metals with suitable work functions are selected as positive and negative electrodes of the device, respectively. Both 20 nm Ti and 50 nm Au (300 μm in diameter) were thermally evaporated on the top of the graphene as an anode, and the thermally fused In was contacted to the bottom of SiC as the cathode. The final as-fabricated device whose thickness is 0.36 mm is shown in Figure 2A with a top view image and a schematic diagram (not to scale).
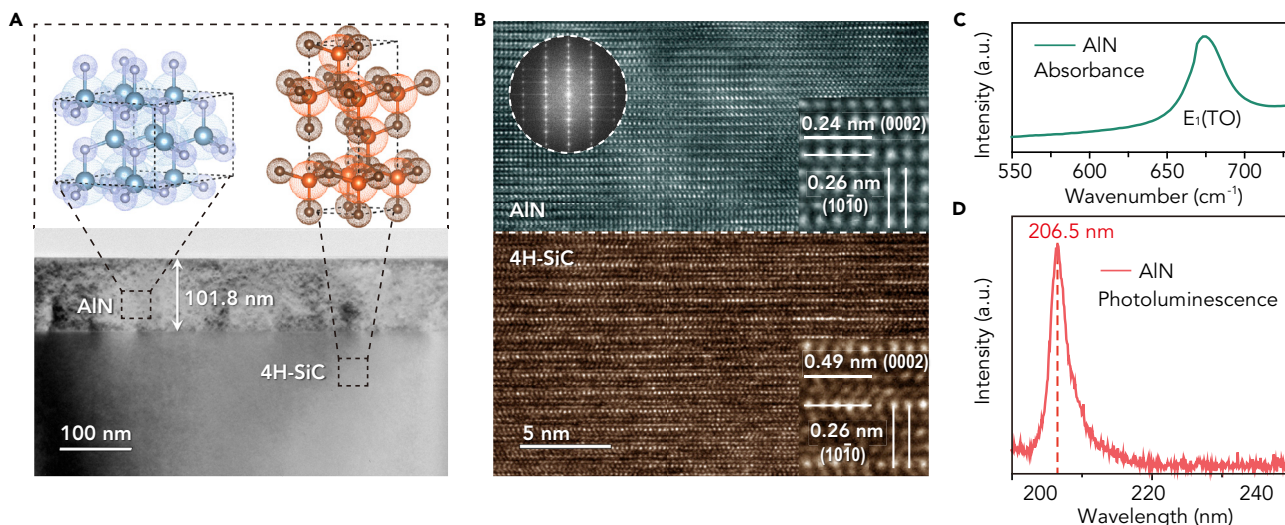
Figure 1. Characterization of Epitaxial AlN Film on 4H-SiC Substrate

(A) Cross-sectional SEM image of AlN/SiC heterojunction and the thickness of the AlN film is approximately equal to 101.8 nm. Inset includes the crystal structure of AlN and 4H-SiC, both of which belong to the *P6₃mc* space group.

(B) HRTEM pattern obtained under near [01$\bar{1}$0] zone axis of AlN and 4H-SiC lattice at interface, and the corresponding Fast Fourier Transform image is displayed in the upper left corner. The lower right corner is a magnified view of the crystal lattice. The interplanar spacing of the (0002) plane of AlN and the (0004) plane of 4H-SiC are both about 0.24 nm, whereas the (10$\bar{1}$0) planes are both about 0.26 nm.

(C) Infrared absorption spectra of AlN. The E_1 transverse vibration (TO) mode of infrared activity of AlN can be observed.

(D) Photoluminescence spectrum of AlN film, with luminescent center at 206.5 nm, suggesting selective absorption characteristics for VUV light. The excitation wavelength is 193 nm.

See also Figure S1.

Photovoltage Output Measurements

Figure 2B is the I-V characteristic curve of the device in dark state, which visually shows the unidirectional conduction effect of the heterojunction. The high crystallinity and high resistance state of the AlN absorber layer are attested by the extremely low dark current (about 10^{-10} A at reverse bias of -4 V) and the noise voltage density (Figure 2C), which is almost covered by the background noise of the equipment used for testing. We measured the photocurrent of the device by using a low-pressure mercury lamp (185 nm monochrome light) as a VUV light source. Under the irradiation of 185 nm VUV light (276.2 μW/cm^2), owing to the efficient collection of photo-generated carriers by two charge-selective layers, the device generates a large open-circuit voltage of up to 2.45 V between the two electrodes and the potential on the p-Gr side is higher than that on the n-SiC side (Figure 2D). At 0 V bias, the light/dark current ratio exceeds six orders of magnitude, certifying the ultra-high signal-to-noise ratio of the device and its excellent VUV responsivity in current detection mode. To further obtain the voltage output characteristics of the device, we performed a voltage-time curve test (Figure 2E), which embodies the stable voltage output of the device with a bias current of zero. The average output voltage is 2.454 V within 100 s. It should be noted that we have measured three identical devices to obtain reliable experimental results. Error bars in Figure 2E represent SD from three independent devices. Although the measured values of the individual devices are slightly different, for a certain device, an almost constant open-circuit voltage can always be reproduced and stabilized for a long time (Figure S3). To prove that photo-generated carriers are mainly accumulated at both ends of graphene and SiC in the open-circuit state, the I-V characteristics of contacts formed by SiC and graphene contacted with the electrodes have been measured (Figure S4). A perfect ohmic contact indicates that the voltage drop at the metal-semiconductor contact is much less than that of the device itself. The results presented here preliminarily demonstrate the efficient band assembly and the reliable electrical signal output characteristics of the device.

Ideal Model for Open-Circuit Voltage

As shown in Figure 3A, compared with different types of heterojunction PV devices previously reported (Si [Green et al., 2019; Kanneboina et al., 2018; Masuko et al., 2014; Yoshikawa et al., 2017], GaAs [Beattie et al., 2018; Gruginskie et al., 2018; Ho et al., 2018; Outes et al., 2018], perovskite [Jaysankar et al., 2019; Jeon et al., 2018; Luo et al., 2018; Stolterfoht et al., 2018], AlN [Zheng et al., 2018a, 2018b, 2019]), the
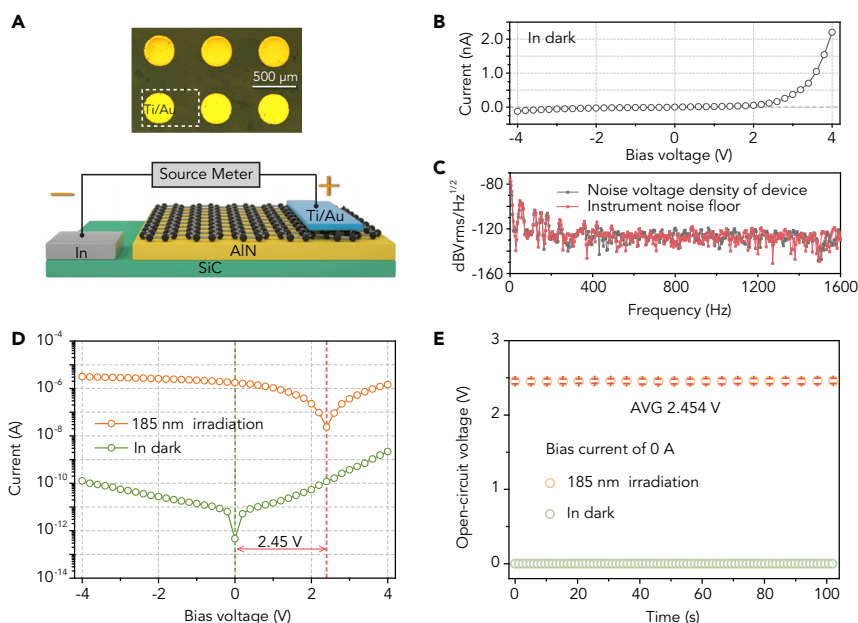
Figure 2. Device Structure and Voltage Output Characteristics
(A) Top view image and schematic diagram of the device structure (not to scale).
(B) I-V output characteristics of the device in dark state, which reveals the unidirectional conduction characteristics of the constructed heterojunction.
(C) The noise voltage density of the device at 0–1600 Hz.
(D) The dark current and the I-V curves under 185 nm monochromatic light irradiation (276.2 μW/cm^2).
(E) The voltage output characteristics under 185 nm monochromatic light irradiation (276.2 μW/cm^2) at bias current of 0 A.
Error bars represent SD from three independent devices.
See also Figures S2–S4.

as-fabricated device attains the highest open-circuit voltage so far. To explore the mechanism of the ultra-high open-circuit voltage generated in this device, the carrier distribution and transport characteristics of the heterojunction in different states need to be analyzed profoundly. The bulk and contact features of the functional layers in the heterojunction are shown in Figure 3B. The conduction band minimum (E_C) and valence band maximum (E_V) of the wurtzite-type AlN are located at the central Γ point of Brillouin zone, with a direct energy band gap of approximately 6.2 eV (Zoroddu et al., 2001), and 4H-SiC is an indirect band gap semiconductor with a band gap of ~3.23 eV (Park et al., 1994). The gray line represents the vacuum level, and the electron affinity of AlN and 4H-SiC is 1.4 and 3.1 eV, respectively. Since the values of the effective mass of electrons and holes are different, the Fermi level of the intrinsic AlN slightly deviates from the center of the band gap, which is about 4.44 eV. And the Fermi level of the heavily doped n-SiC is very close to the conduction band minimum (about 3.17 eV) (see Transparent Methods). In addition, the Fermi level of graphene is below the Dirac point (~4.56 eV) (Giovannetti et al., 2008), indicating a low density of states as a hole transport layer. Under thermal equilibrium, the entire heterojunction has a uniform Fermi level owing to the redistribution of electrons and holes, and two built-in electric fields in the same direction are formed at both interfaces of the heterojunction.

Under VUV irradiation, photons with energy equal to or greater than the AlN bandgap are absorbed, and the photo-excited electrons enter the conductive band from the valence band, leaving the same large number of holes behind. Thus, the total electron and hole concentrations (n and p) under irradiation deviate from their thermodynamic equilibrium values (n_0 and p_0) in dark state, which can be described by quasi-Fermi levels E_{Fn} and E_{Fp} (see Transparent Methods). These negative (electron) and positive (hole) charge carriers first reach the space charge region by diffusion and then drift to the SiC electron transport layer and the graphene hole transport layer, respectively, under the influence of the built-in electric field to generate photo-generated current. The current density is almost zero when the circuit is open (the reverse photocurrent is equal to the forward diffusion current), so the quasi-Fermi level of electrons and holes is constant and must be equal to the potential at the contact. This means that the difference in $E_{Fn}-E_{Fp}$ is constant throughout the device and is equal to the voltage applied when the circuit is open.
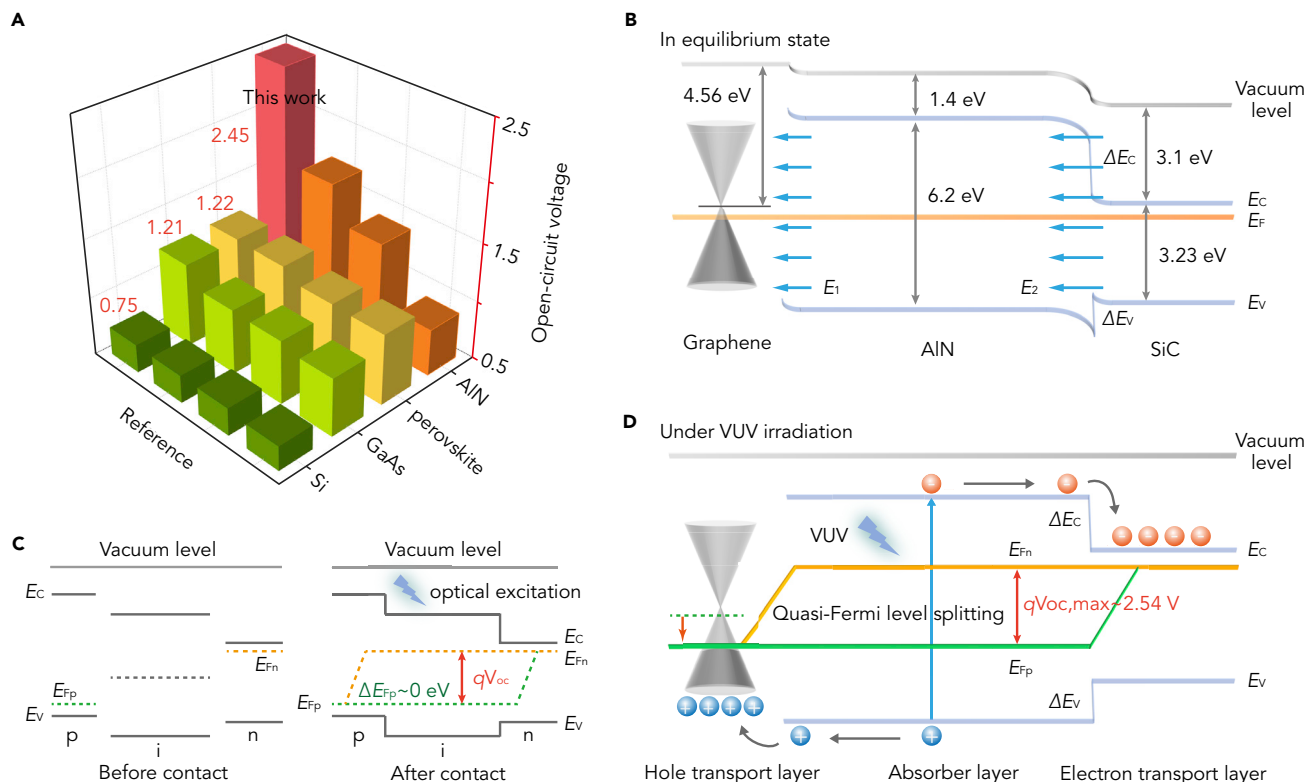
Figure 3. Generation Mechanism of the Ultra-high Open-Circuit Voltage

(A) Comparison of open-circuit voltages of different types of PV devices, including Si, GaAs, and perovskite.

(B) Schematic diagram of the energy band of the p-Gr/i-AlN/n-SiC heterojunction in thermal equilibrium. Two built-in electric fields (blue arrows) of the same direction are formed in the space charge region at both interfaces of the heterojunction.

(C) Bulk characteristics of functional layers of common p-i-n heterojunctions and their energy band diagrams under photo-excitation. In general, the maximum open-circuit voltage that can be obtained depends on the difference between the Fermi levels of the *p*-type and *n*-type regions.

(D) Schematic diagram of the energy band in the non-equilibrium state under VUV irradiation. The orange and green lines indicate the maximum split $qV_{oc,max}$ (~2.54 V) of the quasi-Fermi level of electrons and holes, which depends on the AlN/SiC junction with a large contact potential difference. And the Fermi level of graphene is pulled down under irradiation. At this point, the potential in the semiconductor is substantially flat.

In general, both the *p*-type and *n*-type regions of a common p-i-n heterojunction device have large doping concentration. Figure 3C (left) shows the bulk characteristics of the functional layers when they are not in contact with each other. The Fermi levels of the *p*-type and *n*-type regions are close to the top of the valence band and the bottom of the conduction band, respectively. When all functional layers are contacted to form a heterojunction, the maximum open-circuit voltage that can be obtained by the device under illumination depends on the difference between the Fermi levels of the *p*-type and *n*-type regions, as manifested in Figure 3C (right). In other words, the splitting of the quasi-Fermi level in the heterojunction is limited by the carrier concentration of the *p*-type and *n*-type regions. This is because the carriers generated by optical excitation in the absorber layer are not sufficient to change the bulk characteristics of the *p*-type and the *n*-type regions (that is, the Fermi level is substantially unchanged). However, because graphene, as a hole transport layer, is close to the eigenstate, its Fermi level could be pulled down when there is a large amount of hole injection. Therefore, we consider that the maximum open-circuit voltage that the device can generate is limited by the contact potential difference between AlN and n-SiC rather than by graphene.

The V_{OC} of the final device is now largely defined by the quasi-Fermi level split of the AlN/SiC heterojunction with a large contact potential difference, and also, in an ideal state, for an approximately intrinsic AlN absorber layer, $n_0 = p_0$, so $n \approx p$ (Carrier recombination is almost neglected). Therefore, $E_{Fn} - E_F \approx E_F - E_{Fp}$ can be obtained, which means the quasi-Fermi level changes of electrons and holes are approximately the same, hence the maximum open-circuit voltage that the device can generate (Figure 3D) could be described by the following formula:
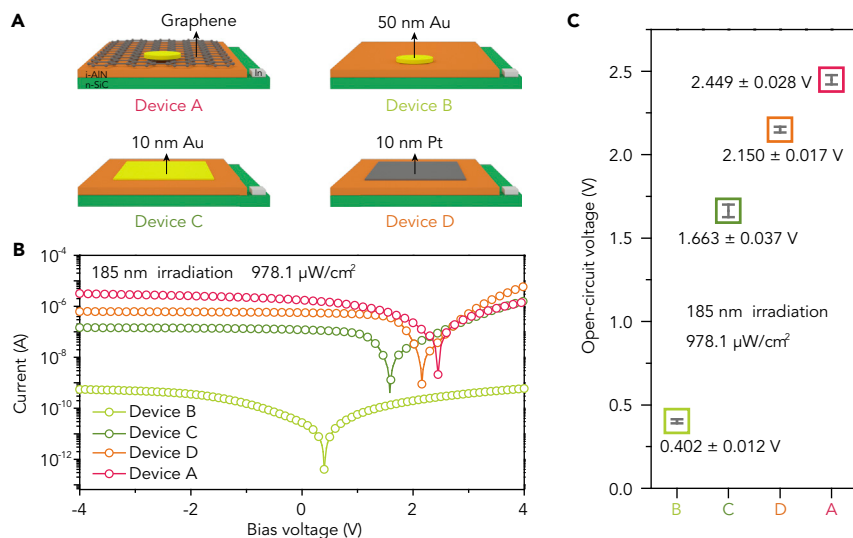
Figure 4. Comparison with Graphene-free Devices
(A) Schematic diagram of four types of devices (not to scale). Device B, C, and D are graphene-free devices.
(B) I-V characteristics of four types of devices under 185 nm light irradiation (978.1 μW/cm^2).
(C) Open-circuit voltages of four types of devices. Error bars represent SD from three independent devices.
See also Figure S5.

$$V_{OC,max} = \frac{E_{Fn} - E_{Fp}}{q} \approx \frac{2(E_{Fn} - E_F)}{q}$$

Substituting the corresponding data into the above formula, the calculated value of $V_{OC,max}$ is approximately equal to 2.54 V. The above is the theoretical value of the open-circuit voltage obtained by the ideal model analysis without considering the surface state and carrier recombination, which is close to the true measurement. Some reports have investigated the charge transfer process between graphene and semiconductors (such as transition metal dichalcogenides), demonstrating the difference between graphene and traditional bulk semiconductors in the aspect of charge transport characteristics (Massicotte et al., 2016; Zhang et al., 2019; Zhu et al., 2015). In this hybrid device, since the transfer of dominant carrier to graphene belongs to hole injection, the density of graphene's hole states increases significantly, resulting in the Fermi level being pulled down under irradiation (Figure 3D), which is consistent with what was reported previously.

Comparison with Graphene-free Devices

To further demonstrate the critical role of quasi-Fermi level splitting enhanced effect achieved by graphene, we prepared three graphene-free devices for comparison (the prototype device is labeled Device A). First, we deposited 50 nm Au directly onto the AlN film by thermal evaporation as shown by Device B in Figure 4A. Obviously, the low photocurrent and open-circuit voltage exhibited by Device B directly demonstrate the efficient collection of carriers by the graphene transparent electrode (Figure 4B). To obtain a larger contact potential difference than that of device A, Au (~5.1eV) and Pt (~5.65eV) with large work functions are selected to form Schottky junctions with the AlN absorber layer. Considering the absorption of VUV light by metal electrodes, 10 nm Au and Pt are deposited on AlN as translucent electrodes (59% and 62% transmittance to 185 nm UV light, respectively, Figure S5), as shown by Device C and Device D in Figure 4A. Device C and Device D exhibit open-circuit voltages of 1.59 and 2.16 V, respectively, which are smaller than that of device A (Figure 4B). It should be noted that 185 nm monochromatic light with a power density of 978.1 μW/cm^2 was used for photoresponse measurements to ensure that the response signal of the devices is saturated. We have prepared three devices of each kind, which are measured under the same conditions. The measurement results are shown in the form of error bars in Figure 4C, from which it can be seen that Device A has the highest photoelectric conversion efficiency. We attribute the ultra-high open-circuit voltage generated by the device to efficient band assembly with following three aspects: (1) An efficient band distribution allows the photo-generated carriers to be efficiently extracted. (2) Graphene has a band structure of a Dirac cone, so its Fermi level near the Dirac point can be changed to give the device

output a larger photo-generated voltage. (3) High crystal quality of AlN reduces trap-assisted recombination via the absorber layer, and good lattice matching of SiC and AlN also greatly suppresses minority carrier recombination at the absorber/transport layer interfaces.

VUV Photodetection Performance

The VUV detection performance of the device has also been systematically tested (see Transparent Methods). By using the self-built VUV spectroscopy measurement system (Figure S6), the spectral responsivity ($R(\lambda) = I_{ph}/P_{opt}$, where I_{ph} is the photocurrent and P_{opt} is the incident light power [Peng et al., 2013]) of the device from VUV to deep UV range at 0 V bias has been obtained (Figure 5A). The results clearly reveal that the PV device possesses a peak responsivity of 79.6 mA/W at 194 nm and a very sharp cutoff wavelength around 205 nm. As shown in the inset of Figure 5A, the corresponding external quantum efficiency (EQE = $hcR/e\lambda$, where h is Planck constant, c the speed of light, e the electron charge, and λ the wavelength of the incident light) is up to 50.96% and the EQE reached a maximum of 56.1% at 172 nm. The VUV/UV-C rejection ratio is as high as 10^4, demonstrating the device's remarkable VUV selective responsivity. Compared with the currently reported PDs based on ultra-wide bandgap semiconductor films (Balducci et al., 2005; Li et al., 2006; Soltani et al., 2008; Zheng et al., 2018a, 2018b), the PV device achieves the highest EQE in Figure 5B, which further indicates the prominent photoelectric conversion capability of the prepared p-Gr/i-AlN/n-SiC heterojunction PV device with high open-circuit voltage.

To explore the signal output characteristics of the device, a power-dependent measurement of the device has been implemented in Figure 5C. As the light power increases, the open-circuit voltage rises rapidly and then gradually reaches the saturation value of 2.45 V. From Figure 5C we have extracted the respective relationship between the short-circuit current and the light power in Figure 5D. The short-circuit current of the device is almost linear with the light intensity, whereas the corresponding photoresponsivity remains nearly the same, which indicates the linear output characteristics and uniform photo-response of the device in the photovoltaic mode. The trend of open-circuit voltage with light power can be fitted with the logistic model in Figure S7A. Under certain VUV irradiation, the output photovoltage of the device can maintain stability for a long time (Figure S7B). When the VUV light source is repeatedly switched, the output photocurrent of the device can always be well reproduced (Figure 5E).

Ultra-fast response speed is an essential requirement for real-time dynamic detection and imaging of solar activity (Zheng et al., 2019). It should be noted that the response speed of the device cannot be observed from Figure 5E because it is limited by the switch speed of the lamp source. The 193-nm nanosecond pulse was utilized to simulate an ultra-fast changing VUV source. The time-dependent photoresponse of the device under VUV pulse irradiation is a reliable reflection of the device's stability to fast changing external signals (Figure S8). The rise time and decay time of the device are 45 ns and 5 μs respectively, which can be obtained from the amplified pulse signal (Figure 5F). It is well known that the rise time of heterojunction PV PDs is mainly limited by the carrier transit time. Thanks to the reasonable design of the depletion layer width and also the high carrier saturation drift speed, the device achieves ultra-fast response speed while maintaining high quantum efficiency. However, the pulse signal output by the device has a relatively obvious tailing phenomenon (decay time is much longer than rise time), which is generally caused by the existence of trap levels in the semiconductor band gap (Zheng et al., 2018b). Nevertheless, the response speed of the device has been greatly improved compared with that of the previously reported VUV PDs (Table S1). The device performance presented here proves that the design of the p-i-n heterojunction structure not only effectively reduces the dark current, but also optimizes both EQE and response speed.

In summary, taking full advantage of the quasi-Fermi level splitting enhanced effect achieved by graphene, the potential difference between the two ends of the device is greatly enhanced. Owing to the efficient band assembly and the growth of high-quality single-crystal thin films, the fabricated device has realized ultra-high open-circuit voltage (~2.45 V) and excellent VUV detection performance compared with different types of PV devices. The test results of three graphene-free devices further demonstrate the importance of efficient band assembly for obtaining high-performance PV devices. This work to some extent provides a valuable reference for the development of PV devices with high open-circuit voltage, sensitivity, stability, and fast response speed and explores the great application prospect of PV devices in space detection.
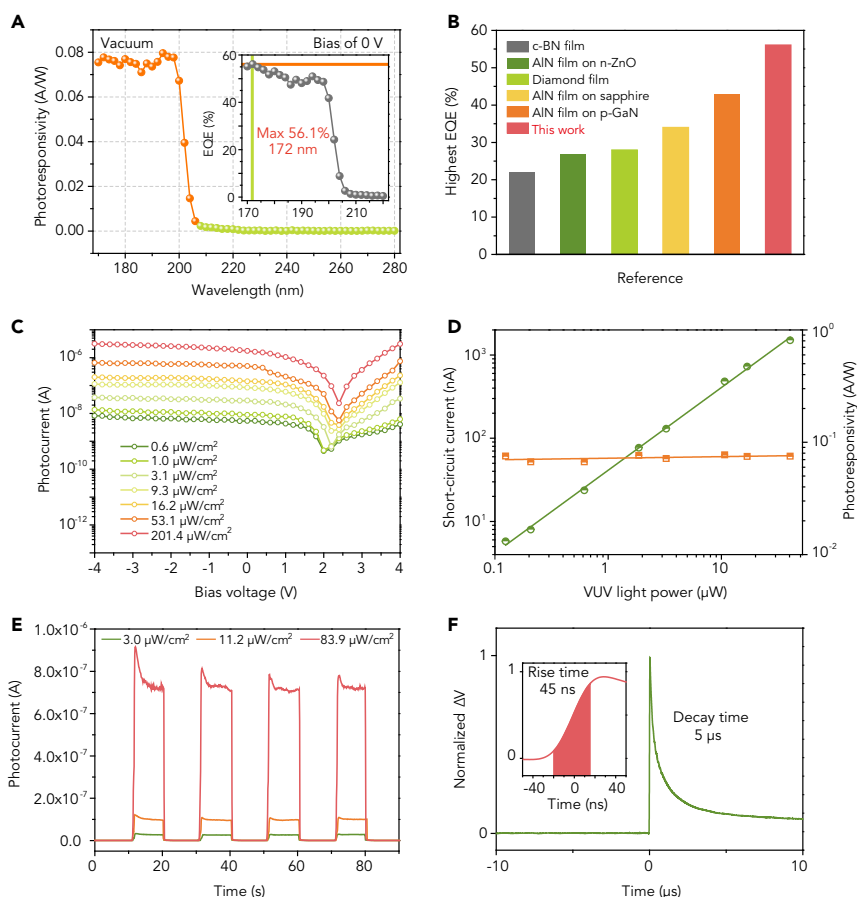
Figure 5. VUV Photodetection Performance of the Device

(A) Photoresponsivity of the device at different wavelengths at 0 V bias and corresponding external quantum efficiency (inset).

(B) Comparison of the highest external quantum efficiency of different semiconductor-based VUV PDs, which is a key indicator for measuring the photoelectric conversion capability of a device.

(C) Transfer characteristic measurements under 185 nm VUV irradiation with light power varied from 0.6 to 201.4 $\mu W/cm^2$.

(D) Fit curve of short-circuit current and responsivity with VUV power, respectively.

(E) Repeated operation of the device in dark state and under 185 nm VUV irradiation of 3.0, 11.2, and 83.9 $\mu W/cm^2$ with zero bias.

(F) Response speed of the device obtained by the amplified impulse response. The rise time and decay time are 45 ns and 5 μs, respectively.

See also Figures S6–S8.

Limitations of the Study

Although the device here, compared with similar ones, has achieved a larger improvement with respect to performance, the optimal process parameters need to be further explored to get the device more stable and closer to the theoretical output. Besides, in this study, the complex interface states and charge transfer processes of graphene and AlN have not been elaborated, which requires more detailed characterization, such as surface potential testing and optical pumping experiments.

METHODS

All methods can be found in the accompanying Transparent Methods supplemental file.

SUPPLEMENTAL INFORMATION

Supplemental Information can be found online at https://doi.org/10.1016/j.isci.2020.100818.

iScience

AUTHOR CONTRIBUTIONS

W.Z. and F.H. conceived and directed this work. L.J. and R.L. fabricated the heterojunction device. L.J., W.Z., and R.L. performed materials characterization. L.J. and R.L. investigated electrical output and photoelectric characteristic. L.J was mainly responsible for data analysis and preparing the manuscript with input from all the other authors.

DECLARATION OF INTERESTS

The authors declare no competing interests.

REFERENCES

Bacaksiz, C., Sahin, H., Ozaydin, H.D., Horzum, S., Senger, R.T., and Peeters, F.M. (2015). Hexagonal AlN: dimensional-crossover-driven band-gap transition. Phys. Rev. B *91*, 085430.

Bae, S., Kim, H., Lee, Y., Xu, X., Park, J.-S., Zheng, Y., Balakrishnan, J., Lei, T., Ri Kim, H., Song, Y.I., et al. (2010). Roll-to-roll production of 30-inch graphene films for transparent electrodes. Nat. Nanotechnol. *5*, 574.

Baker, D., Kanekal, S., Li, X., Monk, S., Goldstein, J., and Burch, J. (2004). An extreme distortion of the Van Allen belt arising from the 'Hallowe'en'solar storm in 2003. Nature *432*, 878.

Baker, D.N. (2002). How to cope with space weather. Science *297*, 1486.

Balducci, A., Marinelli, M., Milani, E., Morgada, M.E., Tucciarone, A., Verona-Rinati, G., Angelone, M., and Pillon, M. (2005). Extreme ultraviolet single-crystal diamond detectors by chemical vapor deposition. Appl. Phys. Lett. *86*, 193509.

Battaglia, C., Cuevas, A., and De Wolf, S. (2016). High-efficiency crystalline silicon solar cells: status and perspectives. Energy Environ. Sci. *9*, 1552–1576.

Beattie, N., See, P., Duchamp, M., Farrer, I., Ritchie, D.A., Tomic, S., and Zoppi, G.. (2018). Quantum engineering InAs/GaAs single-junction concentrator solar cells (Conference Presentation), Vol. 10527 (SPIE).

BenMoussa, A., Hochedez, J.F., Dahal, R., Li, J., Lin, J.Y., Jiang, H.X., Soltani, A., Jaeger, J.-C.D., Kroth, U., and Richter, M. (2008). Characterization of AlN metal-semiconductor-metal diodes in the spectral range of 44–360nm: photoemission assessments. Appl. Phys. Lett. *92*, 022108.

BenMoussa, A., Soltani, A., Gerbedoen, J.C., Saito, T., Averin, S., Gissot, S., Giordanengo, B., Berger, G., Kroth, U., De Jaeger, J.C., et al. (2013). Developments, characterization and proton irradiation damage tests of AlN detectors for VUV

solar observations. Nucl. Instrum. Methods Phys. Res. B *312*, 48–53.

BenMoussa, A., Soltani, A., Schühle, U., Haenen, K., Chong, Y.M., Zhang, W.J., Dahal, R., Lin, J.Y., Jiang, H.X., Barkad, H.A., et al. (2009). Recent developments of wide-bandgap semiconductor based UV sensors. Diam. Relat. Mater. *18*, 860–864.

Bonaccorso, F., Colombo, L., Yu, G., Stoller, M., Tozzini, V., Ferrari, A.C., Ruoff, R.S., and Pellegrini, V. (2015). Graphene, related two-dimensional crystals, and hybrid systems for energy conversion and storage. Science *347*, 1246501.

Brauer, G., Anwand, W., Nicht, E.M., Kuriplach, J., Šob, M., Wagner, N., Coleman, P.G., Puska, M.J., and Korhonen, T. (1996). Evaluation of some basic positron-related characteristics of SiC. Phys. Rev. B *54*, 2512–2517.

Braune, M., Brenner, G., Dziarzhytski, S., Juranic, P., Sorokin, A., and Tiedtke, K. (2016). A non-invasive online photoionization spectrometer for FLASH2. J. Synchrotron Radiat. *23*, 10–20.

Das Sarma, S., Adam, S., Hwang, E.H., and Rossi, E. (2011). Electronic transport in two-dimensional graphene. Rev. Mod. Phys. *83*, 407–470.

Giovannetti, G., Khomyakov, P.A., Brocks, G., Karpan, V.M., van den Brink, J., and Kelly, P.J. (2008). Doping graphene with metal contacts. Phys. Rev. Lett. *101*, 026803.

Green, M.A., Hishikawa, Y., Dunlop, E.D., Levi, D.H., Hohl-Ebinger, J., Yoshita, M., and Ho-Baillie, A.W.Y. (2019). Solar cell efficiency tables (Version 53). Prog. Photovolt. *27*, 3–12.

Gruginskie, N., van Laar, S.C.W., Bauhuis, G., Mulder, P., van Eerden, M., Vlieg, E., and Schermer, J.J. (2018). Increased performance of thin-film GaAs solar cells by rear contact/mirror patterning. Thin Solid Films *660*, 10–18.

Ho, W.-J., Bai, W.-B., Liu, J.-J., and Shiao, H.-P. (2018). Efficiency enhancement of single-junction

GaAs solar cells coated with europium-doped silicate-phosphor luminescent-down-shifting layer. Thin Solid Films *660*, 651–656.

Jaysankar, M., Raul, B.A.L., Bastos, J., Burgess, C., Weijtens, C., Creatore, M., Aernouts, T., Kuang, Y., Gehlhaar, R., Hadipour, A., et al. (2019). Minimizing voltage loss in wide-bandgap perovskites for tandem solar cells. ACS Energy Lett. *4*, 259–264.

Jeon, N.J., Na, H., Jung, E.H., Yang, T.-Y., Lee, Y.G., Kim, G., Shin, H.-W., Il Seok, S., Lee, J., and Seo, J. (2018). A fluorene-terminated hole-transporting material for highly efficient and stable perovskite solar cells. Nat. Energy *3*, 682–689.

Kanneboina, V., Madaka, R., and Agarwal, P. (2018). High open circuit voltage c-Si/a-Si:H heterojunction solar cells: influence of hydrogen plasma treatment studied by spectroscopic ellipsometry. Solar Energy *166*, 255–266.

Li, J., Fan, Z.Y., Dahal, R., Nakarmi, M.L., Lin, J.Y., and Jiang, H.X. (2006). 200nm deep ultraviolet photodetectors based on AlN. Appl. Phys. Lett. *89*, 213510.

Li, L., Liu, X., Pal, S., Wang, S., Ober, C.K., and Giannelis, E.P. (2017). Extreme ultraviolet resist materials for sub-7 nm patterning. Chem. Soc. Rev. *46*, 4855–4866.

Li, X., Zhu, Y., Cai, W., Borysiak, M., Han, B., Chen, D., Piner, R.D., Colombo, L., and Ruoff, R.S. (2009). Transfer of large-area graphene films for high-performance transparent conductive electrodes. Nano Lett. *9*, 4359–4363.

Luo, D., Yang, W., Wang, Z., Sadhanala, A., Hu, Q., Su, R., Shivanna, R., Trindade, G.F., Watts, J.F., Xu, Z., et al. (2018). Enhanced photovoltage for inverted planar heterojunction perovskite solar cells. Science *360*, 1442–1446.

Massicotte, M., Schmidt, P., Vialla, F., Schädler, K.G., Reserbat-Plantey, A., Watanabe, K., Taniguchi, T., Tielrooij, K.-J., and Koppens, F.H. (2016). Picosecond photoresponse in van der

Waals heterostructures. Nat. Nanotechnol. 11, 42.

Masuko, K., Shigematsu, M., Hashiguchi, T., Fujishima, D., Kai, M., Yoshimura, N., Yamaguchi, T., Ichihashi, Y., Mishima, T., Matsubara, N., et al. (2014). Achievement of more than 25% conversion efficiency with crystalline silicon heterojunction solar cell. IEEE J. Photovolt. 4, 1433–1435.

Michel, J., Liu, J., and Kimerling, L.C. (2010). High-performance Ge-on-Si photodetectors. Nat. Photon. 4, 527.

Novoselov, K.S., Fal'ko, V.I., Colombo, L., Gellert, P.R., Schwab, M.G., and Kim, K. (2012). A roadmap for graphene. Nature 490, 192.

Outes, C., Seoane, N., Almonacid, F., Fernández, E.F., and García-Loureiro, A.J. (2018). Study of GaAs vertical solar cells at high concentration levels. Paper presented at: 2018 Spanish conference on electron devices (CDE).

Ouyang, B., Zhang, K., and Yang, Y. (2018). Photocurrent polarity controlled by light wavelength in self-powered ZnO nanowires/SnS photodetector system. iScience 2, 86.

Park, C.H., Cheong, B.-H., Lee, K.-H., and Chang, K.J. (1994). Structural and electronic properties of cubic, 2H, 4H, and 6H SiC. Phys. Rev. B 49, 4485–4493.

Peng, L., Hu, L., and Fang, X. (2013). Low-Dimensional nanostructure ultraviolet photodetectors. Adv. Mater. 25, 5321–5328.

Richter, M., Kroth, U., Gottwald, A., Gerth, C., Tiedtke, K., Saito, T., Tassy, I., and Vogler, K. (2002). Metrology of pulsed radiation for 157-nm lithography. Appl. Opt. 41, 7167–7172.

Shea, M.A., Smart, D.F., McCracken, K.G., Dreschhoff, G.A.M., and Spence, H.E. (2006). Solar proton events for 450 years: the Carrington event in perspective. Adv. Space Res. 38, 232–238.

Soltani, A., Barkad, H.A., Mattalah, M., Benbakhti, B., Jaeger, J.-C.D., Chong, Y.M., Zou, Y.S., Zhang, W.J., Lee, S.T., BenMoussa, A., et al. (2008). 193nm deep-ultraviolet solar-blind cubic boron nitride based photodetectors. Appl. Phys. Lett. 92, 053501.

Sorokin, A.A., Bican, Y., Bonfigt, S., Brachmanski, M., Braune, M., Jastrow, U.F., Gottwald, A., Kaser, H., Richter, M., and Tiedtke, K. (2019). An X-ray gas monitor for free-electron lasers. This article will form part of a virtual special issue containing papers presented at the PhotonDiag2018 workshop. J. Synchrotron Radiat. 26, 1092–1100.

Stolterfoht, M., Wolff, C.M., Márquez, J.A., Zhang, S., Hages, C.J., Rothhardt, D., Albrecht, S., Burn, P.L., Meredith, P., Unold, T., et al. (2018). Visualization and suppression of interfacial recombination for high-efficiency large-area pin perovskite solar cells. Nat. Energy 3, 847–854.

Tsukazaki, A., Ohtomo, A., Onuma, T., Ohtani, M., Makino, T., Sumiya, M., Ohtani, K., Chichibu, S.F., Fuke, S., Segawa, Y., et al. (2004). Repeated temperature modulation epitaxy for p-type doping and light-emitting diode based on ZnO. Nat. Mater. 4, 42.

Wood, J.D., Schmucker, S.W., Lyons, A.S., Pop, E., and Lyding, J.W. (2011). Effects of polycrystalline Cu substrate on graphene growth by chemical vapor deposition. Nano Lett. 11, 4547–4554.

Xu, X., Chen, J., Cai, S., Long, Z., Zhang, Y., Su, L., He, S., Tang, C., Liu, P., Peng, H., et al. (2018). A real-time wearable UV-radiation monitor based on a high-performance p-CuZnS/n-TiO2 photodetector. Adv. Mater. 30, 1803165.

Yoshikawa, K., Kawasaki, H., Yoshida, W., Irie, T., Konishi, K., Nakano, K., Uto, T., Adachi, D., Kanematsu, M., Uzu, H., et al. (2017). Silicon heterojunction solar cell with interdigitated back contacts for a photoconversion efficiency over 26%. Nat. Energy 2, 17032.

Zhang, L., Chen, Z., Zhang, R., Tan, Y., Wu, T., Shalaby, M., Xie, R., and Xu, J. (2019). Direct observation of charge injection of graphene in the graphene/WSe2 heterostructure by optical-pump terahertz-probe spectroscopy. ACS Appl. Mater. Interfaces 11, 47501–47506.

Zheng, W., Huang, F., Zheng, R., and Wu, H. (2015). Low-Dimensional structure vacuum-ultraviolet-sensitive (λ < 200 nm) photodetector with fast-response speed based on high-quality AlN micro/nanowire. Adv. Mater. 27, 3921–3927.

Zheng, W., Lin, R., Jia, L., and Huang, F. (2019). Vacuum ultraviolet photovoltaic arrays. Photon. Res. 7, 98–102.

Zheng, W., Lin, R., Ran, J., Zhang, Z., Ji, X., and Huang, F. (2018a). Vacuum-ultraviolet photovoltaic detector. ACS Nano 12, 425–431.

Zheng, W., Lin, R., Zhang, D., Jia, L., Ji, X., and Huang, F. (2018b). Vacuum-ultraviolet photovoltaic detector with improved response speed and responsivity via heating annihilation trap state mechanism. Adv. Opt. Mater. 6, 1800697.

Zheng, W., Lin, R., Zhang, Z., and Huang, F. (2018c). Vacuum-ultraviolet photodetection in few-layered h-BN. ACS Appl. Mater. Interfaces 10, 27116–27123.

Zheng, W., Lin, R., Zhu, Y., Zhang, Z., Ji, X., and Huang, F. (2018d). Vacuum ultraviolet photodetection in two-dimensional oxides. ACS Appl. Mater. Interfaces 10, 20696–20702.

Zhu, X., Monahan, N.R., Gong, Z., Zhu, H., Williams, K.W., and Nelson, C.A. (2015). Charge transfer excitons at van der Waals interfaces. J. Am. Chem. Soc. 137, 8313–8320.

Zoroddu, A., Bernardini, F., Ruggerone, P., and Fiorentini, V. (2001). First-principles prediction of structure, energetics, formation enthalpy, elastic constants, polarization, and piezoelectric constants of AlN, GaN, and InN: comparison of local and gradient-corrected density-functional theory. Phys. Rev. B 64, 045208.

Supplemental Information

Ultra-high Photovoltage (2.45 V) Forming

in Graphene Heterojunction via Quasi-Fermi Level

Splitting Enhanced Effect

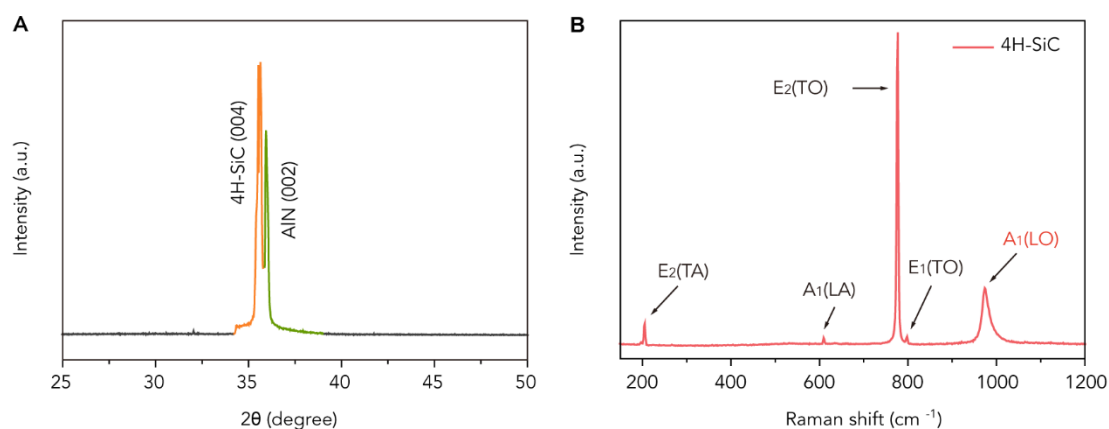Lemin Jia, Wei Zheng, Richeng Lin, and Feng Huang

Figure S1 Characterization of AlN/SiC heterojunction, related to Figure 1.

(A) XRD pattern of *c*-plane AlN grown on 4H-SiC substrate. The highly symmetric (002) diffraction peak of AlN and the clear (004) diffraction peak of SiC verifies that both AlN and SiC grow along the *c*-axis.

(B) Raman spectrum of n-type 4H-SiC. Compared to the intrinsic SiC, the planar mode is unchanged, while the A_1 Raman band is asymmetrically broadened and shifted due to an increase in electron concentration. The A_1 (LO) mode of intrinsic SiC is at about 965 cm^{-1}, while in this figure it is observed at 974 cm^{-1}. The narrow full width at half maximum of the in-plane vibration mode in the 4H-SiC Raman spectrum reflects the long phonon lifetime of the crystal, while the A_1 longitudinal optical (LO) mode has an asymmetric broadening and frequency shift compared to the intrinsic SiC, identifying n-type doping of SiC(Chafai et al., 2001).
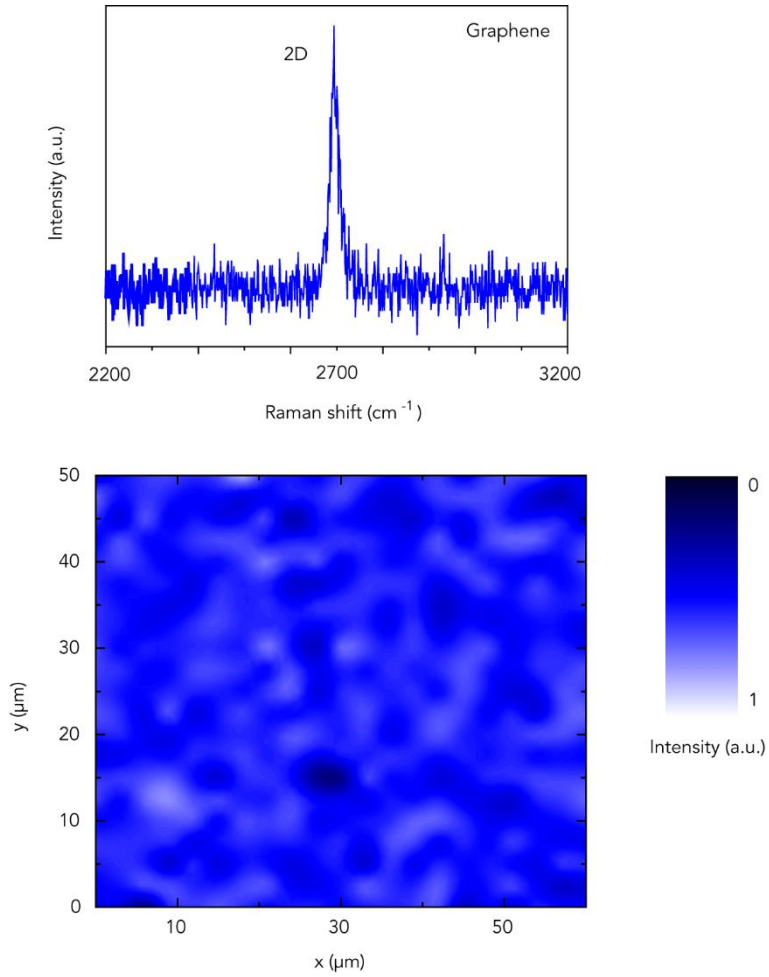
Figure S2 Raman mapping of graphene on AlN film, related to Figure 2.
It proves the spatial uniformity of graphene window layer (Intensity at point of 2700 cm^{-1}, 50 μm×60 μm).
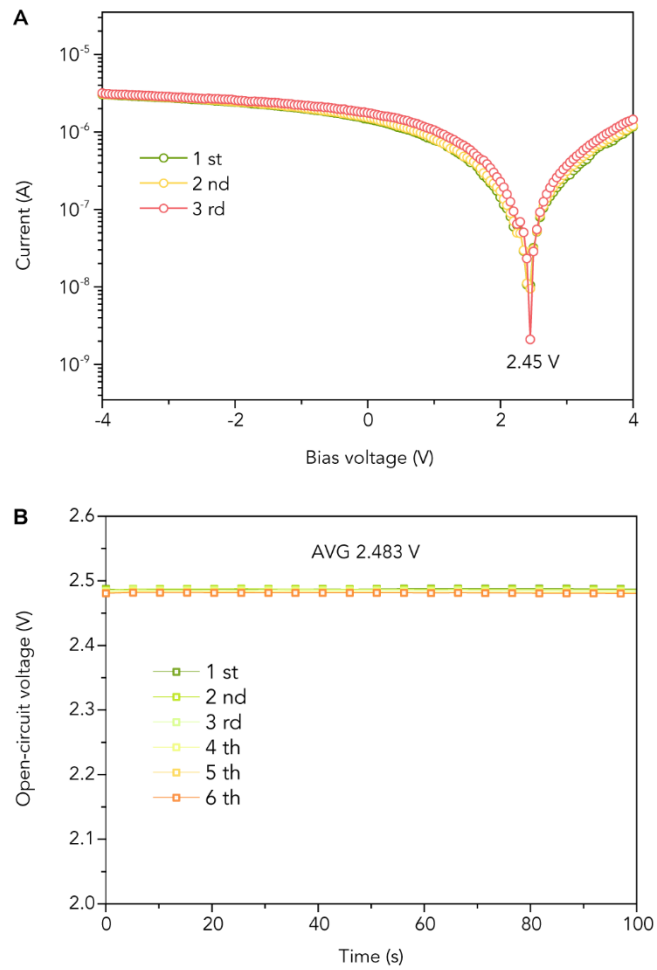
Figure S3 Cyclic stability of maximum output voltage, related to Figure 2.

(A) The open-circuit voltage of the device is 2.45 V for three times by scanning the I-V curve.

(B) The V-T curve scanning of the device for six times. The average output voltage within 600 s is 2.483 V.
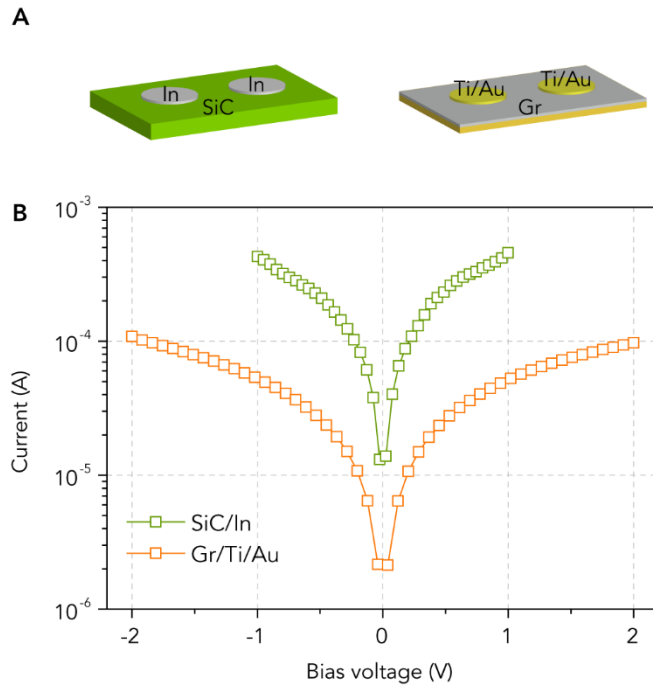
Figure S4 Ohmic contact test of SiC/In and Gr/Ti/Au, related to Figure 2.

(A) Schematic diagram of the ohmic contact test.

(B) I-V characteristic curves of the ohmic contacts formed by SiC and graphene contacted with the electrodes.
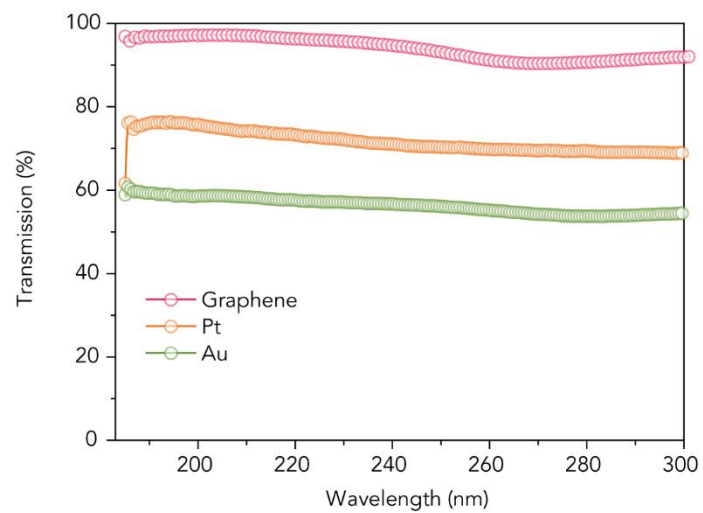
Figure S5 Transmission spectrum of transparent conductive layers, related to Figure 4.
The transmittance of graphene, Au (10 nm) and Pt (10 nm) to 185 nm VUV light is 96.9%, 61.6% and 59.1%, respectively.
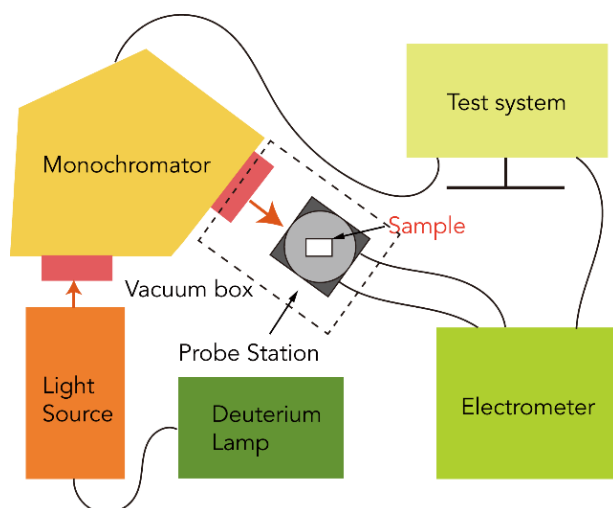
Figure S6 Schematic diagram of VUV spectroscopy measurement system, related to Figure 5. The VUV spectral response test system is built by ourselves including an IHR320 (Horiba) deep-UV with a diffraction grating of 1200 grooves mm^{-1} at 250 nm, a 200 W deuterium lamp source L11798 (Hamamatsu), a vacuum box, and a Keithley 6517B source meter to measure photocurrent. The monochromatic light power was calibrated using a VXUV20A photodetector (PTO Diode Corp).
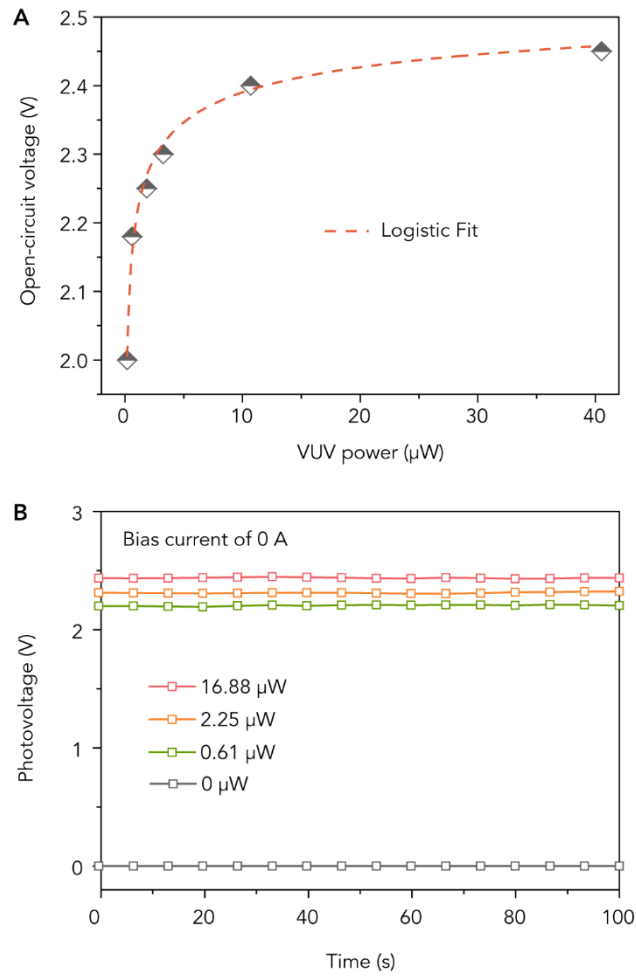
Figure S7 The power-dependent measurements, related to Figure 5.
(A) Fit curve of open-circuit voltage with VUV power. The trend of open-circuit voltage with light power can be fitted with the logistic model, which conforms to the characteristics of photovoltaic devices.
(B) Stable output of open-circuit voltage at different VUV powers. Under certain VUV irradiation, the output photovoltage of the device can maintain stable for a long time.
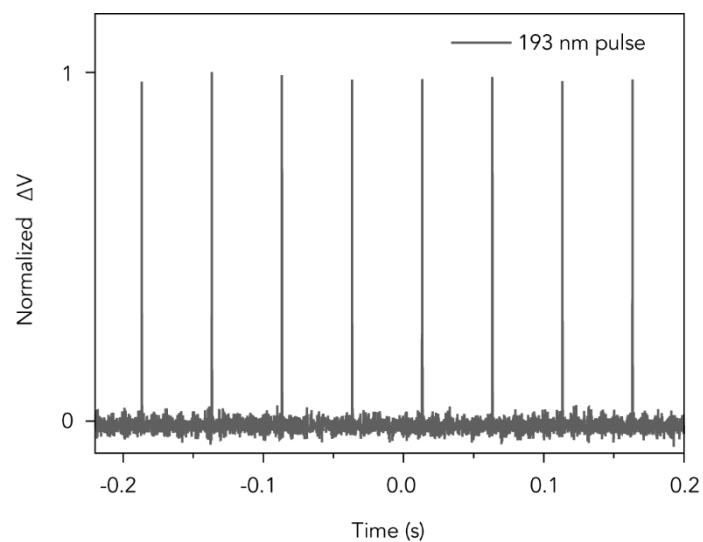
Figure S8 Voltage output signal of the device generated under continuous equally-interval 193-nm ns pulse, related to Figure 5.

The interval of the pulse signal is 9 ns. An oscilloscope was uesd for collection of high-speed variation output voltage signal.

Table S1 Comparison of response time of VUV photodetectors based on AlN film, related to Figure 5.

Material	Rise time (s)	Decay time (s)	Reference
AlN film	< 8	< 3	(Li et al., 2006)
Gr/AlN/GaN	8×10^{-8}	4×10^{-4}	(Zheng et al., 2018a)
Gr/AlN/ZnO	4.2×10^{-6}	1×10^{-3}	(Zheng et al., 2018b)
Gr/AlN/Si	1.2×10^{-7}	2×10^{-3}	(Zheng et al., 2019)
Gr/AlN/SiC	4.5×10^{-8}	5×10^{-6}	This work

Transparent Methods

Material synthesis

Epitaxial growth of AlN on n-4H-SiC was conducted by using a production MOCVD with capacity of 56 pcs. MOCVD could optimize the interface between the absorber layer and the electron transport layer. At a low pressure of 200 Torr and a temperature of 1050 °C, the AlN film was grown at a rate of 100 nm/h, and the final film thickness is about 100 nm. N-type conductive 4H-SiC is a commercially available standard wafer and the Si surface is polished. The electron density of the SiC wafer is about 10^{18} cm^{-3}, and the conductivity is about 0.02 Ω/cm. The graphene window layer is high-quality commercial Gr/Cu sample by chemical vapor deposition (CVD). Detailed growth methods can be found in Reference(Wood et al., 2011).

Material characterization

The SEM images were obtained by ZEISS AURIGA's field emission scanning electron microscope. Tecnai G2 F30 of FEI (300 kV) equipped with high resolution transmission electron microscopy (HRTEM) was used for analyzing crystal structure. X-ray diffraction, and Raman spectroscopy were performed using Panalytical X'Pert Pro X-ray diffractometer with Cu-Kα radiation (λ = 1.5406 Å) and Renishaw in Via reflex micro Raman with 488 nm pump laser, respectively. Infrared absorption spectra of AlN film was obtained by IRAffinity-IS Fourier Transform Infrared Spectrometer of SHIMADZU. And its VUV photoluminescence spectra was obtained using Exacted ArF excimer lasers, EX5/250 mini excimer Laser, and GAM LASER, and the spectral acquisition was dependent on the QE65PRO Scientific-Grade spectrometer with H70 grating (200−289 nm).

Device fabrication

For device A, after obtaining an epitaxial AlN film on a 4H-SiC single crystal substrate, a 2 × 2 mm graphene grown by CVD was formed on the AlN surface via a wet transfer method as a transparent conductive window. The specific experimental process is as follows. First, a layer of PMMA (~300 nm) was spin-coated on Gr/Cu. Then, heat treatment was performed at 70 °C for 10 minutes to enhance the adhesion of PMMA to graphene. Next, the copper foil is etched away using an ammonium nitrate solution. The Gr/PMMA film was washed in deionized water to remove residual ions. After transferring Gr/PMMA immersed in deionized water to AlN/SiC, the samples were dried at 80 °C for 5 minutes. Finally, the samples were immersed in acetone to dissolve PMMA, and the residual ions were removed by deionized water. The electrodes at both ends of the device are constructed by different methods. 20 nm Ti and 50 nm Au (300 μm in diameter) were thermally evaporated on top of the graphene as the positive electrode, and the thermally fused In was contacted to the bottom of SiC as the negative electrode. For device B, 50 nm Au (300 μm in diameter) were thermally evaporated on top of the clean AlN surface directly. For device C and D, 10 nm Au and Pt (1 × 2 mm) were deposited on top of the clean AlN surface by ion sputtering method, respectively.

Electrical measurements

The I-V characteristic curves were measured using a 4200A-SCS source meter (Keithley) with Clarius software by Voltage Linear Scan Mode. The sample is placed in a vacuum probe station (Lakeshore) for measurement. VUV light source (185 nm monochromatic light) is provided by a low-pressure mercury lamp equipped with quartz glass. The change in light power is achieved by

adjusting the distance between the light source and the device. The time-current relationship curves were tested in voltage bias mode (0 V). And the time-voltage relationship curves were measured in the current bias mode (0 A). The switch curves were obtained by manually switching the light source at the same time interval. The response speed of the device cannot be read from the curve because it is limited by the switch speed of the lamp source. The noise voltage density of the device was obtained using Stanford SR785.

Spectral response measurement

The spectral response test utilized a self-built VUV spectral response test system, including an IHR320 (Horiba) deep-UV with a diffraction grating of 1200 grooves mm^{-1} at 250 nm, a 200 W deuterium lamp source L11798 (Hamamatsu), a vacuum box for placing samples, and a Keithley 6517B source meter to measure photocurrent. It should be noted that the monochromatic light power was calibrated using a VXUV20A photodetector (PTO Diode Corp). Light power of different wavelength can be obtained by spectral response and responsivity curves of standard Si photodetector.

Temporal response measurement

A self-assembled VUV impulse response test system was constructed to measure response time of the device. The system includes an ArF excimer laser as a pulsed source, an EX5/250 micro-excimer laser (GAM laser), and a Keysight DSOS604A 6G oscilloscope for collection of high-speed variation output voltage signal. The interval of the pulse signal is 9 ns.

Calculation of theoretical values of Fermi levels

The theoretical value of the Fermi level of the intrinsic AlN can be calculated by formula

$$E_F = \frac{E_C + E_V}{2} + \frac{3k_0 T}{4} \ln \frac{m_p^*}{m_n^*}$$

where k_0 is the Boltzmann constant, T the thermodynamic temperature, m_p^* the effective hole mass of density of states, m_n^* the effective electron mass of density of state. For AlN at 300 K, m_p^* = 7.26 m_0 and m_n^* = 0.4 m_0. Therefore, the calculated $E_{F,AlN} \approx 4.44 eV$.

The theoretical value of Fermi level of n-doped SiC can be calculated by formula

$$E_F = E_C + k_0 T \ln \frac{n_0}{N_C}$$

where N_C is the effective density of states in the conduction band and n_0 is the electron density. For SiC at 300 K, N_C is about 1.7×10^{19} cm^{-3} and n_0 is about 10^{18} cm^{-3}. Therefore, the calculated $E_{F,SiC} \approx 3.17 eV$.

Calculation of quasi-Fermi level splitting

The quasi-Fermi level of the heterojunction under illumination can be described by the following formula(Battaglia et al., 2016).

$$n = n_0 + \Delta n = N_C \, exp(-\frac{E_c - E_{Fn}}{k_0 T}) = n_0 \, exp(\frac{E_{Fn} - E_F}{k_0 T})$$

$$p = p_0 + \Delta p = N_V \, exp(-\frac{E_{Fp} - E_V}{k_0 T}) = p_0 \, exp(\frac{E_F - E_{Fp}}{k_0 T})$$

n and p is the total electron and hole concentrations, Δn and Δp the unbalanced carrier concentrations, N_C and N_V the effective state density of the conduction band and the valence band respectively, and E_F is the Fermi level under thermal equilibrium without photo-excited. When the recombination of carriers is not considered, $\Delta n = \Delta p$. Therefore, $E_{\text{Fn}} - E_F \approx E_F - E_{\text{Fp}}$ can be obtained which means the quasi-Fermi level changes of electrons and holes are approximately the same, hence the maximum open- circuit voltage that the device can generate could be described by the following formula.

$$V_{\text{OC,max}} = \frac{E_{\text{Fn}} - E_{\text{Fp}}}{q} = \frac{2(E_{\text{Fn}} - E_F)}{q}$$

Substituting the corresponding data into the above formula, the calculated value of $V_{\text{OC,max}}$ is approximately equal to 2.54 V.

Supplemental References

Battaglia, C., Cuevas, A., and De Wolf, S. (2016). High-efficiency crystalline silicon solar cells: status and perspectives. Energy & Environmental Science 9, 1552-1576.

Chafai, M., Jaouhari, A., Torres, A., Antón, R., Martín, E., Jiménez, J., and Mitchel, W.C. (2001). Raman scattering from LO phonon-plasmon coupled modes and Hall-effect in n-type silicon carbide 4H–SiC. Journal of Applied Physics 90, 5211-5215.